

Optimization of Spatial Resolution and Image Reconstruction Parameters for the Small-Animal Metis™ PET/CT System

Jie Zhao

Xuzhou Medical College

Qiong Liu

Xuzhou Medical College

Chaofan Li

Xuzhou Medical College

Yunfeng Song

Xuzhou Medical College

Ying Zhang

Xuzhou Medical College

Mejia Jose

Universidad Autónoma de Ciudad Juárez

Jyh-Cheng Chen (✉ jyhcheng2010@gmail.com)

Xuzhou Medical College

Research Article

Keywords: image reconstruction, Spatial Resolution, phantom

Posted Date: January 11th, 2022

DOI: <https://doi.org/10.21203/rs.3.rs-1228467/v1>

License: © ⓘ This work is licensed under a Creative Commons Attribution 4.0 International License.

[Read Full License](#)

Optimization of Spatial Resolution and Image Reconstruction Parameters for the Small-Animal MetisTM PET/CT System

Jie Zhao^{1,+}, Qiong Liu^{1,+}, Chaofan Li^{2,+}, Yunfeng Song¹, Ying Zhang¹, Mejia Jose⁵, and Jyh-Cheng Chen^{1,3,4,*}

¹ School of Medical Imaging, Xuzhou Medical University, Jiangsu, 221004, China

² School of Medical Information and Engineering, Xuzhou Medical University, Jiangsu, 221004, China

³ Department of Biomedical Imaging and Radiological Sciences, National Yang Ming Chiao Tung University, Taipei, 11221, Taiwan

⁴ Department of Medical Imaging and Radiological Technology, Yuanpei University of Medical Technology, Hsinchu, 30015, Taiwan

⁵ Department of Electrical and Computer Engineering, Autonomous University of Ciudad Juarez, 32310, Mexico

* Correspondence: Jyh-Cheng Chen; Electronic mails: jyhcheng2010@gmail.com; Telephones: 14768421970, +886-2-2826-7282, +886-3-5381183 ext 7510; Fax: +886-2-2820-1095.

+ Jie Zhao, Qiong Liu and Chaofan Li contributed equally to this work and share first authorship

ABSTRACT

The aim of this study was to investigate the optimization of spatial resolution and image reconstruction parameters related to image quality in an iterative reconstruction algorithm for the small-animal MetisTM PET/CT system. We used a homemade Derenzo phantom to evaluate the image quality by visual assessment, signal-to-noise ratio, contrast, coefficient of variation, and contrast-to-noise ratio of the 0.8 mm hot rods of 8 slices in the centre of the phantom PET images. A healthy mouse study was performed to analyze the influence of optimal reconstruction parameters and Gaussian post-filter FWHM. In the phantom study, the best image quality was obtained by placing the phantom at one end, keeping the central axis parallel to X-axis of the system, selecting iterations between 30 and 40, with a reconstruction voxel of 0.314 mm and a Gaussian post-filter FWHM of 1.57 mm. The optimization of spatial resolution can reach 0.6-mm. In the animal study, it was suitable to choose a voxel size of 0.472-mm, iterations between 30 and 40, and 2.36-mm Gaussian post-filter FWHM. Our results indicate that optimal imaging conditions and reconstruction parameters are necessary to obtain high-resolution images and quantitative accuracy, especially for the high-precision identification of tiny lesions.

Introduction

As a dual-modality medical imaging device, PET/CT is widely used in the diagnosis and treatment planning of diseases. High-resolution small-animal PET/CT plays an important role in preclinical studies because of its high sensitivity and resolution^{1,2}.

Since sensitivity and spatial resolution are an oxymoron, so the trade-off is challenging to achieve and needs to be explored and studied in depth³. The National Electrical Manufacturers Association (NEMA) recommends the use of the unified standard NEMA NU 4-2008 for the performance evaluation of small-animal PET/CT equipment in 2008, specifying the use of low-activity ²²Na point sources for spatial resolution measurement and a filtered back-projection (FBP) algorithm for image reconstruction⁴.

The majority of literature reports that FBP introduces star-like artifacts⁵⁻⁸, and it is not as widely used as iterative reconstruction algorithm at present. Hallen et al. mentioned that a more obvious solution for measuring the spatial resolution of the system is to use the scanner's built-in reconstruction method (usually an iterative reconstruction algorithm) to reconstruct the point source data, which artificially increases the spatial resolution despite its non-negativity and non-linearly constrained nature. Another option is to use a micro Derenzo phantom instead of a low-activity point source and allow the use of the scanner's built-in reconstruction method⁸. The use of Derenzo phantoms with different specifications as auxiliary experiments to evaluate the spatial resolution of the system is a common method used by many scholars⁹⁻¹².

The spatial resolution or image quality obtained using the iterative reconstruction algorithm is limited by the location and orientation of the phantom to be scanned, the accuracy of the system response matrix (SRM) modeling, the number of subsets and iterations of reconstruction, the full width at half maximum (FWHM) of the Gaussian post-filter, and the reconstruction matrix and voxel size. Optimal image reconstruction parameters are necessary for small-animal PET/CT system to improve spatial resolution and quantitative accuracy^{13,14}. In this study, we determined the optimal imaging conditions and reconstruction parameters in terms of image quality and resolution by a homemade Derenzo phantom experiment. Then, we analyzed the impact of the optimal reconstruction parameters on PET imaging in animals.

Results

● Derenzo phantom analysis

Figure 1 shows the analysis of PET images quality of the Derenzo phantom reconstructed by the system's MLEM algorithm for different orientations and positions. PET images with the central axis of the rods parallel to Z-axis of the PET system (Zc, Ze) were not shown here, which were very poor visualized, and only 0.9 mm hot rods could be identified. As the 0.8 mm hot rods were not clearly visible in its PET images, the corresponding image quality analysis of Zc and Ze cannot be performed.

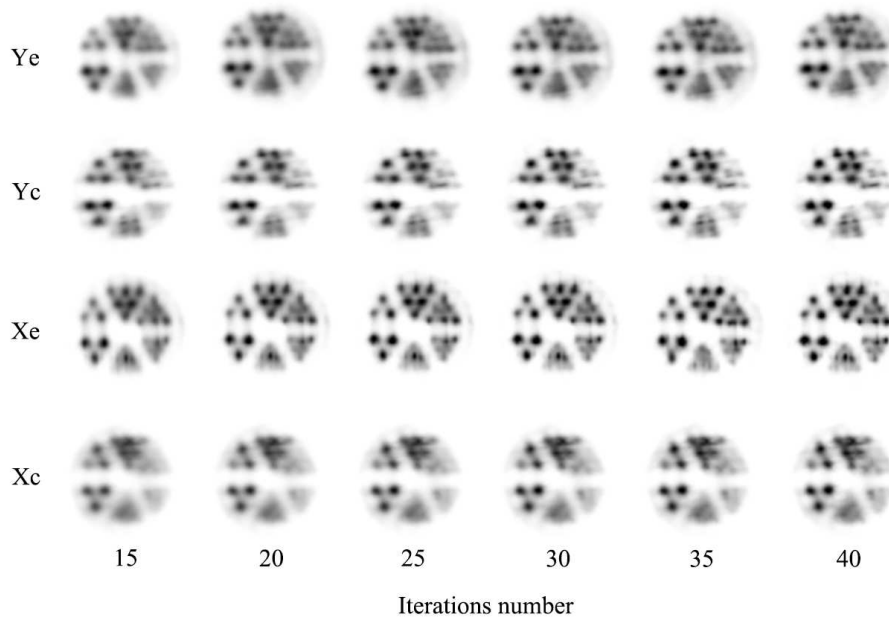


Figure 1. The PET images of the Derenzo phantom reconstructed by MLEM (iteration 40) algorithm in different orientations, positions, and iterations number.

The image quality of Xe in Figure 1 was the best, with a 0.6 mm hot rods visible. For Ye, Yc, and Xc, the smallest identifiable rods were 0.7 mm, 0.8 mm, and 0.8 mm, respectively. SNR, contrast, CV, and CNR were plotted in Figure 2 as a function of the iterations number. In these experiments, the SNR values of Xc were highest between 1 and 25 iterations, with a maximum at iteration 10, followed by Xe with a maximum at iteration 15. Xe, Xc, Ye, and Yc reach convergence roughly at iteration 25. For contrast and CNR analysis, Xe had the highest contrast and CNR values, Xc had the lowest contrast and CNR values, and Ye and Yc were intermediate. As the iteration increases, the CV of the images continues to increase. In all iterations, Xc's image has the smallest CV value, with Ye being second only to it.

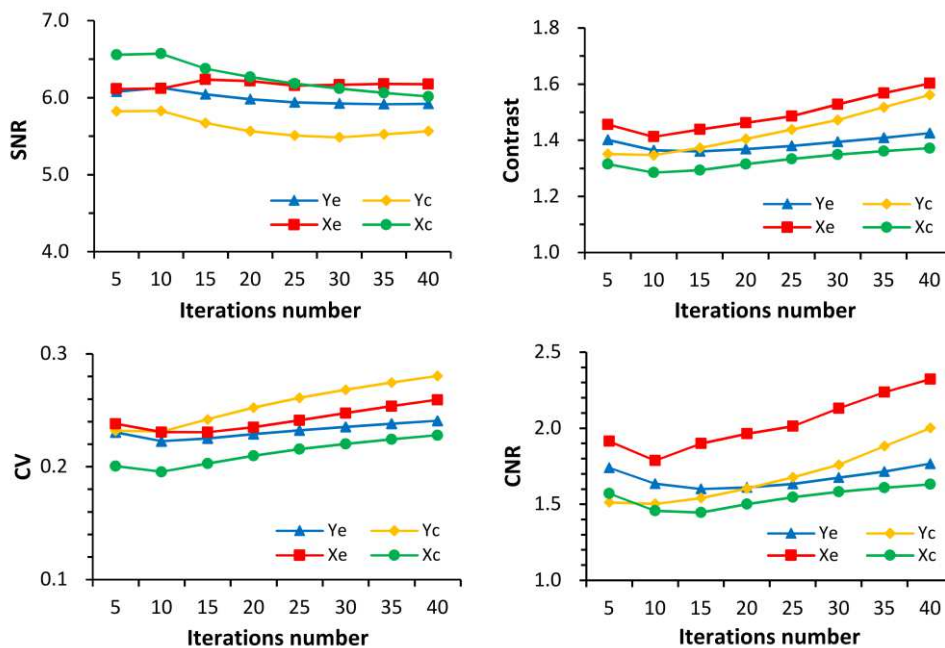


Figure 2. The SNR, Contrast, CV, and CNR of PET images reconstructed by MLEM algorithm in different orientations and positions were plotted as a function of iterations number.

Figure 3 shows the analysis of PET images quality of the Derenzo phantom reconstructed with 3D-OSEM algorithm (subset 5) in different orientations and positions. We also analyzed other PET images reconstructed with multiple subsets using the image quality evaluation metric. The images of Xe can clearly identify the 0.6 mm hot rods, followed by Xc and Ye, which identify 0.7 mm hot rods. Yc has the worst imaging, with only 0.8 mm hot rods visible. Meanwhile, the images of 8 to 12 iterations showed little change for the six sub-experiments from a visual assessment.

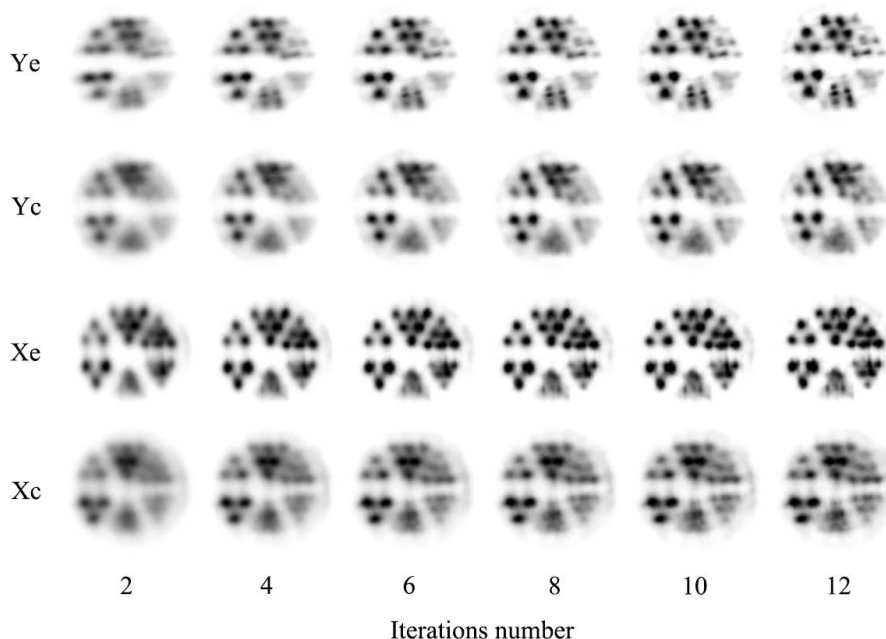


Figure 3. The PET images of the Derenzo phantom reconstructed by 3D-OSEM algorithm (5 subsets, 20 iterations) in different orientations, positions, and iterations number.

Figure 4 shows the change in image quality metrics as the number of iterations increases. For image SNR analysis, Ye has the highest values in these experiments from 4 to 20 iterations, followed by Yc. The SNR values of Yc, Xc, and Xe gradually converge and overlap after 15 iterations. Xe and Xc reached convergence after approximately 6 iterations. Xe has the highest contrast values from 1 to 12 iterations, the highest CNR values from 1 to 7 iterations, and the highest CV values in all iterations, while Yc has the lowest contrast, CV and CNR analysis across all iterations. Results for other multiple subsets of images show that the best images occur at 10 subsets and 3 to 4 iterations, 15 subsets and 2 to 3 iterations, 20 subsets and 2 iterations, 25 subsets and 2 iterations, 30 subsets and 1 iteration. Therefore, we can assume that the optimal resolution and image quality for the Derenzo phantom was at iterative updates from 30 to 40.

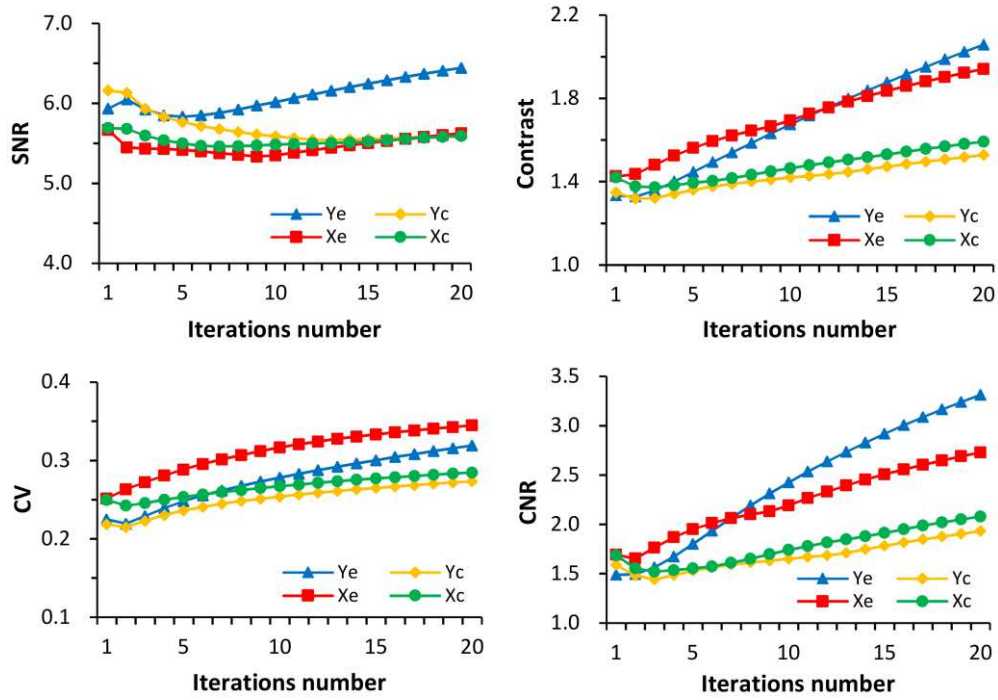


Figure 4. The SNR, Contrast, CV, and CNR of PET images reconstructed by 3D-OSEM algorithm (5 subsets, 20 iterations) in different orientations and positions were plotted as a function of iterations number.

Table 1 shows the time required for the two reconstruction algorithms. 3D-OSEM (subset 5) has an average reconstruction rate of approximately 70.3% higher than MLEM. Figure 5 shows the effect of different Gaussian post-filter FWHMs on PET images of the Derenzo phantom using the MLEM algorithm (iteration 35). Image quality is visually best when applying a Gaussian post-filter of 1.57 mm FWHM, followed by 2.36 mm FWHM.

Table 1. Time required for different iterative updates of 3D-MLEM and 3D-OSEM (5 subsets) algorithms

Iterative updates	Time-3D-MLEM (s)	Time-3D-OSEM (s)	Ratio (%)
5	5	2	60
10	8	3	62.5
15	11	3	72.7
20	14	4	71.4
25	17	5	70.6
30	21	5	76.2
35	24	6	75
40	27	7	74.1

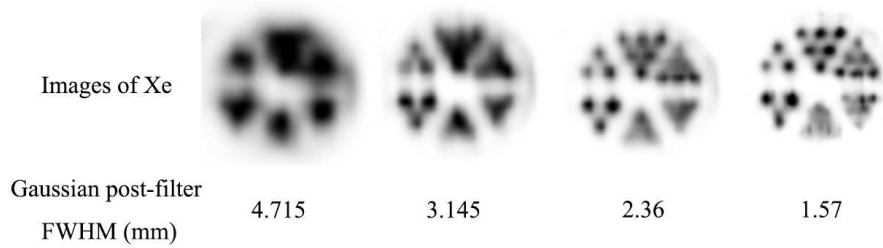


Figure 5. The PET images of the Derenzo phantom of Xe sub-experiment using MLEM algorithm (iteration 35) with different Gaussian post-filter FWHM.

● Animal analysis

The whole-body of a mouse was imaged using the MLEM algorithm with an iteration updates of 35 according to the optimal reconstruction parameters determined by the Derenzo phantom, as shown in Figure 6. The reconstructed voxel size of the PET image in Figure 6(a) was 0.472 mm, with a matrix size of $171 \times 171 \times 259$, and a FWHM of 2.36 mm for the Gaussian post-filter. The reconstructed voxel size of the PET image in Figure 6(b) was 0.314 mm, the matrix size was $257 \times 257 \times 389$, and the Gaussian post-filter FWHM was 1.57 mm. It can be clearly seen that the edges of tissue structures such as brain, heart, and kidney of the mouse in Figure 6(a) were smooth, whereas in Figure 6(b) those were discontinuities, artifacts, and unevenness.

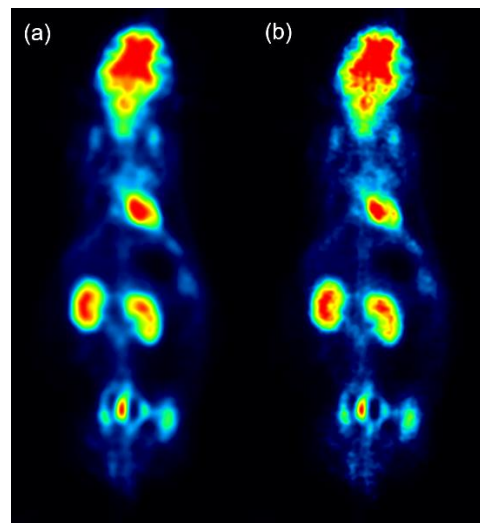


Figure 6. Whole-body PET imaging of a healthy mouse. (a) The reconstructed voxel size was 0.472 mm, and the Gaussian post-filter FWHM was 2.36 mm. (b) The reconstructed voxel size was 0.314 mm, and the Gaussian post-filter FWHM was 1.57 mm.

Discussion

In this study, we evaluated the impact of different imaging conditions and reconstruction parameters in iterative reconstruction algorithms on PET image quality by the Derenzo phantom experiments, and investigate the optimization of spatial resolution and image reconstruction parameters for the small-animal MetisTM PET/CT system. PET image quality and spatial resolution were comprehensively analyzed

through five image evaluation metrics: visual assessment, SNR, contrast, CV, and CNR. Our results show that the PET images gradually become clearer as the number of iterations increases, with the relevant evaluation metrics reaching convergence after 30 iterations. From the visual assessment analysis of Figure 1 and Figure 3, it can be found that placing the phantom at one end of the PET axial FOV and keeping the central axis of the rods parallel to X-axis of the PET system results in the best image quality. We can clearly identify the 0.6 mm hot rods. The PET images where the central axis of the rods parallel to Z-axis of the PET system (Z_c , Z_e) was very poor visualized, and only 0.9 mm hot rods can be identified. Also, the image quality of the Derenzo phantom placed at one end of the PET axial FOV was better than that of the centre because the PET system has four detector rings and the centre of the FOV has no detectors to receive gamma photons. We also found that the images from 8 to 12 iterations did not change much for the six sub-experiments, as shown by the visual assessment in Figure 3.

SNR and CV, contrast and CV are mutually contradictory performance indicators, and the balance between them is affected by iterative updates. A compromise trade-off needs to be found between them to achieve high SNR, high contrast, and low CV¹⁵. As can be seen in Figure 2, the PET images of Xe have the highest SNR, contrast and CNR values after 25 iterations, while Xc had the lowest contrast, CV and CNR. Ye and Yc alternate with intermediate contrast and CNR values. Therefore, the optimal imaging conditions to evaluate the spatial resolution of the system by the Derenzo phantom would be like Xe, which is consistent with the results of the visual assessment, which suggests at least 25 iterations for better image quality.

In Figure 4, Ye had the highest SNR values after 4 iterations, followed by Yc. The SNR values of Yc, Xc, and Xe gradually converged and overlapped after 15 iterations. Xe and Xc reached convergence at about 6 iterations. For the contrast, CV, and CNR analysis, Xe had the highest contrast values from 1 to 12 iterations, the highest CV values in all iterations, and the highest CNR values from 1 to 7 iterations, followed by Ye. In addition to SNR, Xc and Yc showed similar trends in contrast, CV, and CNR analysis. For both CV and CNR analysis, Xc and Ye, Xe and Ye all intersected at approximately 7 iterations. Results for other multiple subsets show that the best images appear at 10 subsets and 3 to 4 iterations, 15 subsets and 2 to 3 iterations, 20 subsets and 2 iterations, 25 subsets and 2 iterations, 30 subsets and 1 iteration. Based on the analysis of these experiments, the optimal number of iterations varies from 6 to 8 when the number of subsets was 5. Therefore, the product of the number of subsets and iterations between 30 and 40 is recommended for optimal image quality.

We compared the reconstruction speed of 3D-MLEM and 3D-OSEM algorithms for Xe sub-experiment, as shown in Table 1. 3D-OSEM (subset 5) was on average nearly 70.3% faster than MLEM, but at the cost of increased image variance (noise level). For example, the CV values of each curve in Figure 4 were generally larger than those of Figure 2. Therefore, adjustments must be made in the selection of the optimal parameters for reconstruction. We also analyzed the effects of different reconstructed voxel sizes and Gaussian post-filter FWHM on image quality. Although increasing the Gaussian post-filter FWHM can effectively reduce image noise, the image was getting blurred and fewer hot rods could be identified^{15,16}. When the reconstructed voxel size

was 0.314 mm and the Gaussian post-filter FWHM was 1.57 mm, the image quality of the Derenzo phantom was the best, followed by 2.36 mm. The image quality was worst when the reconstructed voxel size was 0.943 mm and the Gaussian post-filter FWHM was 4.715 mm. Therefore, we choose 30 to 40 iterative updates, 0.472 mm and 0.314 mm reconstructed voxel sizes, 1.57 mm and 2.36 mm Gaussian post-filter FWHM to reconstruct the whole-body data of the healthy mouse.

For a healthy mouse experiment, we mainly adopted the imaging method as Z_c , as the effective trans-axial FOV of the PET system is 81 mm, which is smaller than the body length of the mouse. The smaller the voxel, the higher the accuracy, but the smaller the soma setting is not the better. As can be seen in Figure 6(a), when the reconstructed voxel size was 0.472 mm, the matrix size was $171 \times 171 \times 259$, and the Gaussian post-filter FWHM was 2.36 mm, the edges of internal tissue structures such as the mouse brain, heart, and kidney were smooth and continuous. The image had significant contrast and no artifacts. However, the PET image in Figure 6(b) were discontinuities, artifacts, and unevenness.

There are two limitations to consider in these analyses. First, the list-mode data of the Derenzo phantom was reconstructed by the iterative algorithms under different imaging conditions to specifically evaluate the optimization of spatial resolution and image reconstruction parameters for the small-animal MetisTM PET/CT system. The results of the evaluation are non-migrating and may not be applicable to other commercial small-animal PET systems, but the evaluation methods can be used as a reference. Secondly, we did not adequately consider the impact of depth effect (DOI) on the spatial resolution of the system. Further investigation is required to perform accurate system modeling to improve PET image quality and resolution.

Methods

● System description

The small-animal MetisTM PET/CT is an advanced system that couples crystal modules formed by four crystal arrays to a silicon photomultiplier (SiPM, HAMAMATSU S13361-3050NE-04) with a light guide, which was developed by Shandong Madic Technology Co., Ltd, as shown in Figure 7. The scanner consists of 32 detector boxes arranged in 4 consecutive octagonal rings with an axial length of 122 mm and a ring diameter of 129 mm (effective imaging trans-axial FOV of 81 mm). Figure 8 shows a single detector box containing two crystal modules, each consisting of an array of four 12×12 LYSO crystals ($0.943 \times 0.943 \times 10$ mm each). The crystal arrays containing the enhanced specular reflector (ESR) optical reflector film inside are placed on a 4×4 SiPM with the crystals centred at a distance of 1.028 mm. Gaps exist in the PET detection boxes, the crystal modules and the crystal arrays, and the crystal sensitivity will be self-normalized by interpolation to reduce the effect of noisy data¹⁷. The default energy window is 350-750 keV.

The system design integrates the scanning control operation and image processing software of the PET scanner into a single PC workstation. Collected data is stored in list-mode mode, and image reconstruction is performed by the three-dimensional

ordered subsets expectation maximization (3D-OSEM) and the maximum likelihood expectation maximization (MLEM), which includes modular trigger dead time correction, coincidence system dead time correction, radionuclide decay correction, detection efficiency, and geometric normalization processing.

Image processing software includes two parts: image reconstruction and image analysis. Image reconstruction contains four different reconstruction settings: (1) Matrix size is $85 \times 85 \times 129$, isotropic voxel size is 0.943 mm; (2) Matrix size is $128 \times 128 \times 194$, isotropic voxel size is 0.629 mm; (3) Matrix size is $171 \times 171 \times 259$, isotropic voxel size is 0.472 mm; (4) Matrix size is $257 \times 257 \times 389$, isotropic voxel size is 0.314 mm. The experiment operator can choose different reconstruction settings depending on the acquisition protocol for different tissues or regions of interest (ROI). Different manufacturers define different image data formats (defined as .mpv format in this study), which are generally packaged into a uniform DICOM data format. Image analysis includes operations such as quantitative or semi-quantitative calculation of digital images, image smoothing and filtering, window width and level adjustment, delineation of ROIs, pharmacokinetics, and time-activity curves (TACs).

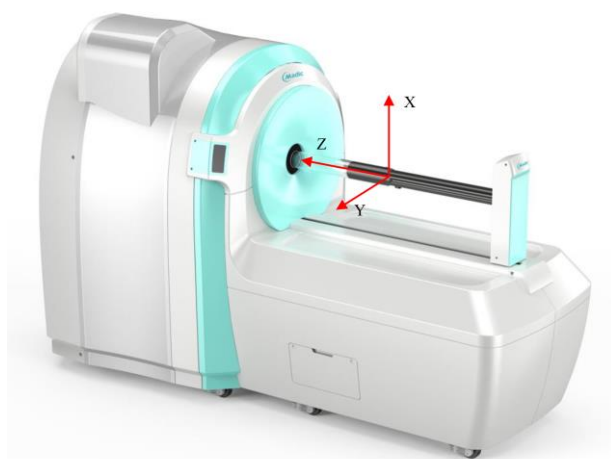


Figure 7. Small-animal Metis™ PET/CT system

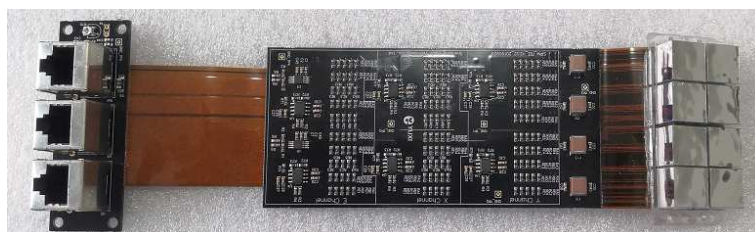


Figure 8. The internal view of a PET detector box, which contains two crystal modules, and each crystal module contains four crystal arrays.

- **Reconstruction algorithm and parameters**

Hudson and Larkin introduced the idea of ordered subsets into the maximum likelihood expectation maximization reconstruction algorithm in 1994¹⁸. The basic principle of OSEM is to divide all projection data into S subsets, which are updated by several iterations to reach image convergence. The list-mode 3D-OSEM algorithm formula can be described as following¹⁹.

$$\lambda_j^{m,l} = \frac{\lambda_j^{m,l-1}}{N_j} \sum_{k \in S_l} p_{i_k j} \frac{A}{s_{i_k} + r_{i_k} + \sum_{b=1}^J p_{i_k b} \lambda_b^{m,l-1}} \quad (1)$$

, where $\lambda_j^{m,l}$ represents the 3D reconstruction image after m iterations and l subsets, and the subscript index of the voxel is $j = 1 \dots J$, S_l indicates that the events are divided into S_l subsets, and the subscript l is the number of the subsets, p_{ij} is the probability that the j -th voxel produces a pair of gamma rays on the i -th response line (LOR), s_{i_k} and r_{i_k} are the scatter and random coincidence coefficients of the LOR where the i_k -th event is located, respectively, A is the correction factor. The calculation formula is as follows.

$$A = \eta_{Decay} \eta_{TrigDeadTime} \eta_{CoincidenceDeadTime} \quad (2)$$

, where η_{Decay} is the radionuclide decay correction coefficient, $\eta_{TrigDeadTime}$ is the crystal modules trigger dead time correction coefficient, and $\eta_{CoincidenceDeadTime}$ is coincidence system dead time correction coefficient.

N_j refers to the sensitivity image of the system, including detector geometric efficiency and tissue attenuation. In fact, the calculation of the sensitivity image is to traverse all possible LORs, for each LOR, calculating its contribution to each voxel. The calculation equation is as follows.

$$N_j = \sum_{i=1}^L \omega_i p_{ij} \quad (3)$$

, where j is the voxel index, i represents the LOR, and L is the total number of LORs. ω_i indicates the normalized weight which contains two parts, one is the detector normalization factor $\eta_{Normalization}$ (including detection efficiency and spatial geometric efficiency), and the other is the attenuation correction coefficient $\eta_{Attenuation}$.

In this study, the double energy window method was mainly used for scatter coincidence correction. The random coincidence correction was accomplished by delaying the coincidence window to obtain random coincidence counts and subtracting them from the actual counts in real time. A Gaussian post-filter with a FWHM of 5 times the voxel size was used as a smoothing filter in all reconstruction models. Meanwhile, the concept tube of response (TOR) was used in the reconstruction process¹⁹, also at 5 times the voxel size.

● Derenzo phantom studies

A homemade small-animal Derenzo phantom with hole diameters of 0.5, 0.6, 0.7, 0.8, 0.9, 1.0 mm was used to measure the spatial resolution of the PET/CT system. The centre-to-centre distance between adjacent rods in the same group was twice the rod diameter. Figure 9 shows an end view of the small-animal Derenzo phantom. The experiment of the phantom consisted of six sub-experiments regarding the injection of fluorine-18 (¹⁸F)-fluorodeoxyglucose (FDG) mixed with saline into the phantom and placed at one end of the scanning bed (as close as possible to the PET axial FOV end, and including the entire Derenzo phantom) or the centre of the PET FOV for data collection, as shown in Table 2.

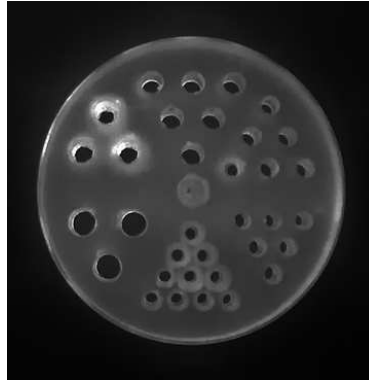


Figure 9. Photograph of the micro Derenzo phantom (end view). The size of the porous array in the Counterclockwise orientation from small to large are 0.5, 0.6, 0.7, 0.8, 0.9, and 1.0 mm. The centre-to-centre distance between adjacent rods is twice the rod diameter.

Table 2. The six sub-experiments on the measurement of PET/CT system spatial resolution by using the Derenzo phantom.

Orientation	Position	Initial activity (MBq)	Acquisition time	Reconstruction algorithms
The central axis of the rods parallel to Z-axis of the PET system	One end (Ze) ¹	3.45	20 min	OSEM / MLEM
	Centre (Zc) ²	3.62	20 min	OSEM / MLEM
The central axis of the rods parallel to Y-axis of the PET system	One end (Ye)	3.71	20 min	OSEM / MLEM
	Centre (Yc)	3.23	20 min	OSEM / MLEM
The central axis of the rods parallel to X-axis of the PET system	One end (Xe)	3.68	20 min	OSEM / MLEM
	Centre (Xc)	3.74	20 min	OSEM / MLEM

¹ Ze means that the Derenzo phantom was placed at one end of the FOV, and the central axis of the rods was kept parallel to the Z-axis of the PET system. ² Zc means that the Derenzo phantom was placed at the centre of the FOV, and the central axis of the rods was kept parallel to the Z-axis of the PET system. Similar for Ye, Yc, Xe, Xc.

The collected data were reconstructed using MLEM and 3D-OSEM algorithms, with iteration ranging from 1 to 40, and subsets ranging from 5 to 20 intervals. The voxel size was 0.314 mm, and the FWHM of the Gaussian post-filter and TOR were both set to 5 times the voxel size. We determined the optimal reconstruction parameters

to interpret the orientation and location of the phantom with the best image quality and resolution. Meanwhile, we compared the reconstruction speed of the best sub-experiment using MLEM and OSEM algorithms.

For the sub-experiment with optimal imaging, we also evaluated the effect of FWHM of the Gaussian-post filter on image quality using MLEM reconstruction algorithm.

● Data analysis methods

The purpose of the data analysis was to evaluate the optimal image conditions and reconstruction parameters, including orientation, position, subsets, iterations, reconstructed voxel size, and Gaussian post-filter FWHM. The analysis of PET images of the Derenzo phantom was performed by visual assessment, signal-to-noise ratio (SNR), contrast, coefficient of variation (CV) and contrast-to-noise ratio (CNR)¹⁵. For the reconstructed PET images, we drew circular ROIs with a diameter of 0.8 mm in each 0.8 mm hot rod centre of 8 slices in the centre of the phantom. We also drew circular ROIs with a diameter of 1.6 mm in each 0.8 mm hot rod centre as the background. The 8 slices in the centre of the phantom need to be judged according to the different orientations and positions of the six sub-experiments.

For visual assessment, the PET images of the Derenzo phantom were evaluated against the smallest hot rods that could be clearly identified. The SNR, contrast, CV and CNR of the 0.8 mm hot rods were used for the quantitative analysis of the Derenzo phantom. The SNR is calculated as follows.

$$SNR = \frac{S_{mean}}{SD} \quad (4)$$

, where S_{mean} is the mean signal intensity of 0.8 mm ROIs in each 0.8 mm hot rod centre of 8 slices in the centre of the phantom, SD is the standard deviation of the background. The contrast, CV and CNR of the 0.8 mm hot rods in the phantom images are calculated as follows, respectively.

$$Contrast = \frac{S_{mean}}{B_{mean}} \quad (5)$$

$$CV = \frac{SD}{B_{mean}} \quad (6)$$

$$CNR = \frac{(S_{mean} - B_{mean})}{SD} \quad (7)$$

, where B_{mean} is the average intensity of 1.6 mm background ROIs.

● Animal study

Animal studies were approved by the Laboratory Animal Ethics Committee of Xuzhou Medical University (Process number for animal experiments: 201706w010). A 40 g, 110 mm long healthy mouse fasted in advance was injected with 18.58 MBq ¹⁸F-FDG via tail vein after induction of anesthesia, which referred to a mixture of oxygen (11/min) and isoflurane (1.5%). Seventy minutes after ingestion, we placed the mouse on the gantry along the Z-axis of the PET system for a 30 minutes whole-body static scanning, and continued to induce anesthesia. We used the optimal reconstruction parameters

from the Derenzo phantom experiments to reconstruct the mouse raw data, and observed the effect of Gaussian post-filter FWHM on mouse imaging. All methods were carried out in accordance with relevant guidelines and regulations. This study was carried out in compliance with the ARRIVE guidelines.

Conclusions

Our results indicate that the optimal imaging conditions and reconstruction parameters are necessary to obtain high-resolution images and quantitative accuracy. In the phantom study, the best image quality was obtained by placing the Derenzo phantom at one end of the PET FOV, keeping the central axis of the phantom parallel to X-axis of the PET system, selecting the number of iterative updates (subsets \times iterations) between 30 and 40, 0.314 mm reconstructed voxel, and 1.57 mm Gaussian post-filter FWHM. In the animal study, it is appropriate to choose a voxel size of 0.472 mm, iterative updates between 30 and 40, and 2.36 mm Gaussian post-filter FWHM for image reconstruction.

Data Availability Statement

The data used to support the findings of this study are available from the corresponding author upon request.

References

1. Yang, Y. *et al.* A Prototype High-Resolution Small-Animal PET Scanner Dedicated to Mouse Brain Imaging. *J. Nucl. Med.* **57**, 1130-1135 (2016).
2. Kuang, Z. *et al.* Performance of a high-resolution depth encoding PET detector using barium sulfate reflector. *Phys. Med. Biol.* **62**, 5945-5958 (2017).
3. DiFilippo, F. P. Design of a Tri-PET collimator for high-resolution whole-body mouse imaging. *Med. Phys.* **44**, 4230-4238 (2017).
4. National Electrical Manufacturers Association. NEMA Standards Publication NU 4 – 2008. Performance Measurements of Small Animal Positron Emission Tomographs. Rosslyn, V A: National Electrical Manufacturers Association; 2008.
5. Oda, K., Toyama, H., Uemura, K., Ikoma, Y. & Senda, M. Comparison of parametric FBP and OS-EM reconstruction algorithm images for PET dynamic study. *Ann. Nucl. Med.* **15**, 417-423 (2001).
6. Frese, T., Rouze, N. C., Bouman, C. A., Sauer, K. & Hutchins, G. D. Quantitative comparison of FBP, EM, and Bayesian reconstruction algorithms for the IndyPET scanner. *IEEE. Trans. Med. Imaging.* **22**, 258-276 (2003).
7. Yu, A. R., Kim, J. S., Kang, J. H. & Lim, S. M. Comparison of reconstruction methods and quantitative accuracy in Siemens Inveon PET scanner. *J. Instrum.* **10**, 1-16 (2015).
8. Hallen, P., Schug, D. & Schulz, V. Comments on the NEMA NU 4-2008 Standard on Performance Measurement of Small Animal Positron Emission Tomographs. *EJNMMI. Phys.* **7**, 1300-1309 (2020).

9. Nagy, K. *et al.* Performance evaluation of the small-animal nanoScan PET/MRI system. *J. Nucl. Med.* **54**, 1825-1832 (2013).
10. Gaudin, É., Toussaint, M., Thibaudeau, C., Paillé, M., Fontaine, R. & Lecomte, R. Performance Simulation of an Ultra-High Resolution Brain PET Scanner Using 1.2-mm Pixel Detectors. *IEEE. Trans. Radiat. Plasma. Med. Sci.* **3**, 334-342 (2019).
11. Pan, T. *et al.* Performance evaluation of the 5-Ring GE Discovery MI PET/CT system using the national electrical manufacturers association NU 2-2012 Standard. *Med. Phys.* **46**, 3025-3033 (2019).
12. Sarnyai, Z., Nagy, K., Patay, G., Molnár, M. & Varrone, A. Performance Evaluation of a High-Resolution Nonhuman Primate PET/CT System. *J. Nucl. Med.* **60**, 1818-1824 (2019).
13. Shekari, M., Ghafarian, P., Ahangari, S., Ghadiri, H., Bakhshayeshkaram, M. & Ay, M. R. Optimizing Image Reconstruction Parameters in Time of Flight PET/CT Imaging: a Phantom Study. *Frontiers. Biomed. Technol.* **2**, 146-154 (2015).
14. Gaitanis, A., Kastis, G. A., Vlastou, E., Bouziotis, P., Verginis, P. & Anagnostopoulos, C. D. Investigation of Image Reconstruction Parameters of the Mediso nanoScan PC Small-Animal PET/CT Scanner for Two Different Positron Emitters Under NEMA NU 4-2008 Standards. *Mol. Imaging. Biol.* **19**, 550-559 (2017).
15. Akamatsu, G. *et al.* Improvement in PET/CT image quality with a combination of point-spread function and time-of-flight in relation to reconstruction parameters. *J. Nucl. Med.* **53**, 1716-1722 (2012).
16. Yoon, H. J., Jeong, Y. J., Son, H. J., Kang, D. Y., Hyun, K. Y. & Lee, M. K. Optimization of the spatial resolution for the GE discovery PET/CT 710 by using NEMA NU 2-2007 standards. *J. Korean. Phys. Soc.* **66**, 287-294 (2015).
17. Baghaei, H., Zhang, Y., Yan, H. & Wong, W. H. Evaluation of a self-normalization method for two PET cameras using prompt, delay or total emission data. Paper presented at: Nuclear Science Symposium & Medical Imaging Conference 2016.
18. Hudson, H. M. & Larkin, R. S. Accelerated image reconstruction using ordered subsets of projection data. *IEEE. Trans. Med. Imaging.* **13**, 601-609 (1994).
19. Prax, G., Chinn, G., Olcott, P. D. & Levin, C. S. Fast, accurate and shift-varying line projections for iterative reconstruction using the GPU. *IEEE. Trans. Med. Imaging.* **28**, 435-445 (2009).

Acknowledgments

We thank Shandong Madic Technology Co., Ltd. for its assistance in the acquisition protocol and the operation of the PET/CT system. We also want to thank the Cancer Institute of Xuzhou Medical University for providing the experimental platform.

Author Contributions

JZ, QL and CL conceived and designed the overall experimental program. QL, CL, YS and YZ carried out experimental work and data analysis. JC contributed to project management. JZ, QL, CL, YS and JC wrote and revised the manuscript. JZ and JC

provided experimental platforms, resources and supervision for the manuscript. All authors read and approved the final manuscript.

Conflicts of Interest

The authors declare that they have no conflict of interest.

Funding

This work was supported by Postgraduate Research & Practice Innovation Program of Jiangsu Province under Grant No. KYCX21_2647; Xuzhou Medical University-Research Cooperation Project under Grant No. KY17012004; Excellent Talents Project of Xuzhou Medical University under Grant No. 53681942; The research project of College Students' Innovation and Entrepreneurship Training Program 202010313064Y; In addition, the project had also received funding support from the General Program of the China Postdoctoral Science Foundation with grant number 2019M651974.